

# AERODYNAMIC ANALYSIS OF HELICOPTER SIDE INTAKE VARIANTS BY FULL SCALE WIND TUNNEL MEASUREMENTS

Dipl.-Ing. F. Knoth\*, Dipl.-Ing. J.H. You\*, Prof. Dr. C. Breitsamter\*

\*Institute of Aerodynamics and Fluid Mechanics, Technische Universität München  
Boltzmannstr. 15, 85748 Garching b. München, Germany

## Abstract

The work presented in this paper aims at the aerodynamic optimization of engine side air intakes of a lightweight helicopter. For this purpose wind tunnel (W/T) tests are conducted on a novel full scale model of a helicopter fuselage section at the Institute of Aerodynamics and Fluid Mechanics of the Technische Universität München (TUM-AER). The new wind tunnel model includes a duct system, venturi meter and a radial fan to provide engine mass flow rates corresponding to realistic helicopter operation conditions. With 5-hole pressure probes significant trends on the total pressure drop and distortion coefficients are found at the Aerodynamic Interface Plane (AIP) for three different air intakes tested in hover and forward flight conditions. Further investigations are conducted concerning local surface pressure distributions.

## 1. NOMENCLATURE

$A$	= cross section
$c_p$	= pressure coefficient
$DC_{60}$	= total pressure distortion coefficient
$\dot{m}$	= mass flow rate
$p$	= static pressure
$q$	= dynamic pressure
$S$	= curve length coordinate
$T$	= static temperature
$U$	= velocity
$W/T$	= wind tunnel
$X$	= X-coordinate
$Y$	= Y-coordinate
$Z$	= Z-coordinate
$\Delta$	= difference
$\eta$	= total pressure ratio
$\rho$	= air density
$\theta$	= circumferential angle in AIP

## Subscripts

$AIP$	= Aerodynamic Interface Plane
$corr$	= corrected value
$ISA$	= ISA conditions at sea level
$low$	= lowest value of 60° sectors in AIP
$max$	= maximum value
$norm$	= normalized value
$Ref$	= value for BSL 1 variant without intake grid at the operation condition $U_\infty/U_{\infty,max} = 0, \quad \dot{m}_{corr}/\dot{m}_{corr,max} = 0.79$
$rel$	= relative
$t$	= total
$\infty$	= ambient condition

## 2. INTRODUCTION

The European Union has launched the CleanSky initiative together with the European aerospace industry aimed at a reduction of emissions and fuel burn. The engine installation plays an important role to foster fuel-efficient engine operation and decrease emissions. The work presented in this paper is part of the ATHENAI (Aerodynamic Testing of Helicopter Novel Air Intakes) project. The ATHENAI project belongs to the Green RotorCraft 2 (GRC2) sub-project within the Clean Sky JTI (Joint Technology Initiative). In the ATHENAI project the aerodynamic optimization of novel engine air intake concepts is conducted at the example of a light twin-engine helicopter with an emphasis on fast forward flight conditions. For this purpose, a new full scale model of a helicopter fuselage section has been designed which allows for the modular exchange of single model components, such as the intake cowling part or the engine plenum chamber. As part of the first wind tunnel campaign of the ATHENAI project a comprehensive database is created for three different side intake concepts. The database is used to understand the influence of the side intake concepts on engine entry parameters such as the total pressure loss and the total pressure distortion. These parameters are evaluated in the AIP (Aerodynamic Interface Plane) by means of a circumferentially adjustable 5-hole pressure probing system. Based on the results of the wind tunnel tests of the first wind tunnel campaign retrofit solutions, such as spoilers and guide vanes, are developed in the second testing period. In the following, the ATHENAI wind tunnel model is presented together with selected results of the first wind tunnel campaign.

### 3. W/T SETUP

All investigations are conducted in the subsonic Göttingen-type wind tunnel facility A of TUM-AER, as shown in Fig. 1. The open test section of the atmospheric wind tunnel measures 1.8 m x 2.4 m x 4.8 m (height x width x length). The maximum velocity of the open test section is  $U_{\infty} = 65$  m/s. The free stream turbulence intensity is below 0.4 %. The uncertainty in the mean velocity distribution in time and space is below 0.7 %. The uncertainty in free stream direction is less than  $0.2^{\circ}$  and static pressure variations are below 0.4 %.

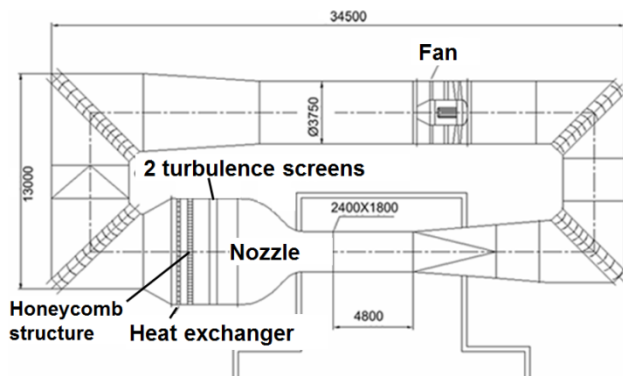


Fig. 1: W/T A facility of TUM [1].

In Fig. 2 the integration of the wind tunnel model is depicted with the subsystems and the adjacent W/T components. The components are listed in Table 1.

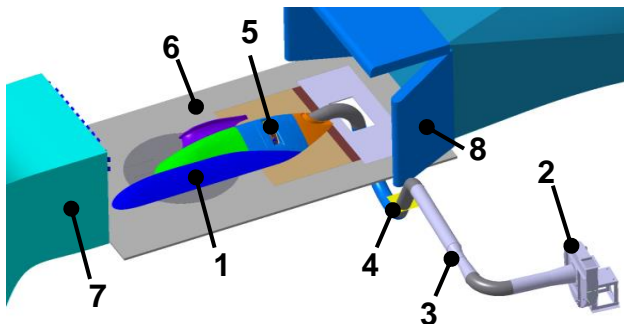


Fig. 2: Overview of the W/T setup.

1	ATHENAI wind tunnel model
2	Radial fan
3	Venturi meter
4	Duct system
5	Air intake section
6	W/T floor
7	W/T nozzle
8	W/T collector

Table 1: Components of W/T model and test set-up.

#### 3.1. W/T model

In order to fulfil local Mach and Reynolds number similarities, a full scale geometry has been

investigated. The outer geometry of the W/T model refers to a fuselage part model. The influence of the tail section on the intake flow field area, which is situated upstream, is considerably small. The main rotor influence and the rotor downwash in level flight are also small for the intake section. The outer geometry is smoothed which means that geometric details on the cabin and cowling like antennas, rivets, screws etc. are not taken into account. Geometric details like the foreign object damage grids that substantially influence the local flow field of the inlet region, are maintained.

The W/T test section as well as nozzle and collector restrict the size of the model examined. First, a constriction of the freestream flow field is to be avoided in the vicinity of the nozzle exit and collector entry. Therefore, an overall size of 4.5 m in the main stream direction shall not be exceeded. Second, due to blockage effects, the height of the model is limited. The blockage is kept at a moderate level of 7-8%. To meet the spatial restrictions, only a truncated section of the cabin and cowling is tested, as shown in Fig. 3 in front view.

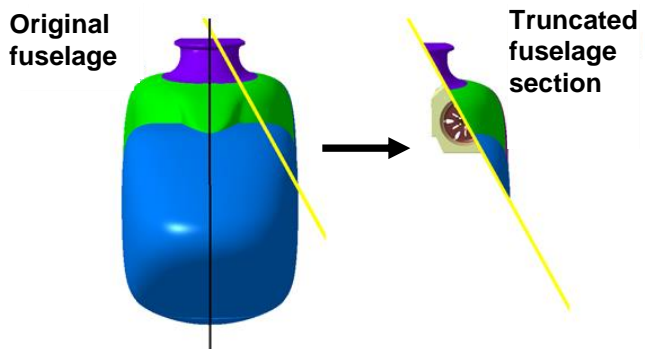


Fig. 3: Truncation of fuselage in front view.

In the following the components of the wind tunnel model shown in Fig. 2 are described in more detail. In Fig. 4, the outer components are presented.

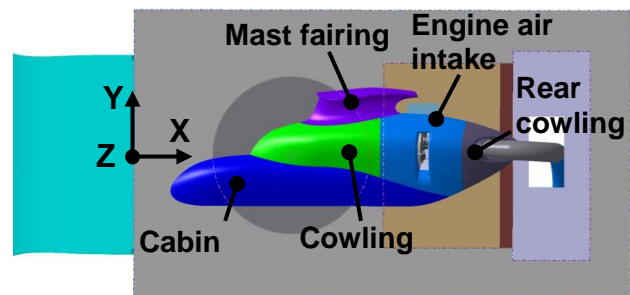


Fig. 4: Outer W/T model components.

Furthermore, the coordinate system used is shown. The point of origin is situated on the bottom of the nozzle in its symmetry plane.

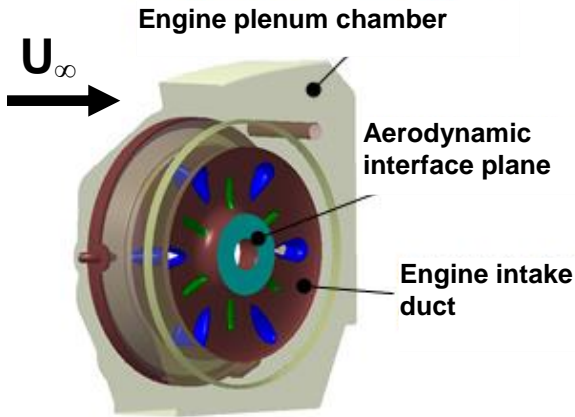


Fig. 5: inner W/T model components.

The inner model components are depicted in Fig. 5. The engine plenum chamber (EPC) is connected to the engine air intake (EAI). It embeds the engine intake duct (EID) which is a nozzle leading to the aerodynamic interface plane (AIP).

Downstream of the AIP, the circular duct is extruded in the direction of the engine's axis and is connected to the fan using two bends and a flexible tube element, see Fig. 2. For the real helicopter, the AIP is located directly upstream of the compressor.

### 3.2. Engine mass flow simulation

As the engine mass flow has an essential effect on the internal flow upstream of the AIP, suitable mass flow rates corresponding to inflight operation conditions are simulated in the wind tunnel. For this purpose a radial fan is connected to the internal components of the model via a duct system. The fan as well as the duct system and its components have been chosen early in the design process of the W/T model taking into account the compensation of total pressure losses created by the intake geometry and the duct system.

A venturi meter, as shown in Fig. 6, is integrated to allow for the measurement of mass flow rates in accordance with Ref. [2]. For the mass flow adjustment the rotation speed of the fan is regulated.

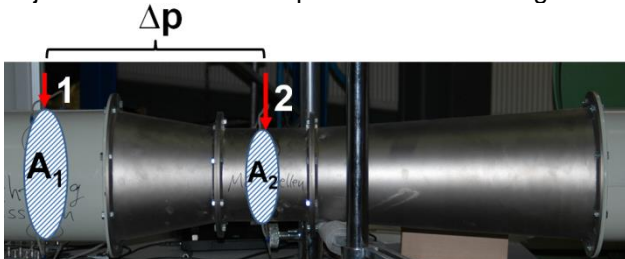


Fig. 6: Venturi meter, measurement plane 1 and 2.

In order to ensure Mach number similarity for the results obtained in the W/T and real flight conditions independent of the ambient conditions due to

weather and heights, the corrected mass flow rate is used as defined in eq. (1).

$$(1) \quad \dot{m}_{corr} = \dot{m} \sqrt{\frac{T_t}{T_{ISA}} \frac{p_{ISA}}{p_t}}$$

Hereby,  $T_{ISA} = 288.15$  K and  $P_{ISA} = 101325$  Pa are the ISA ambient conditions at sea level.  $T_t$  and  $P_t$  are the total temperature and total pressure measured at the wind tunnel nozzle exit, which represent the total ambient flight conditions.

As depicted in Fig. 7, four different mass flow rates are defined as a function of W/T freestream velocity. The mass flow rates 1 – 3 correspond to different power requirements. The mass flow rate 4 is a constant maximum mass flow rate.

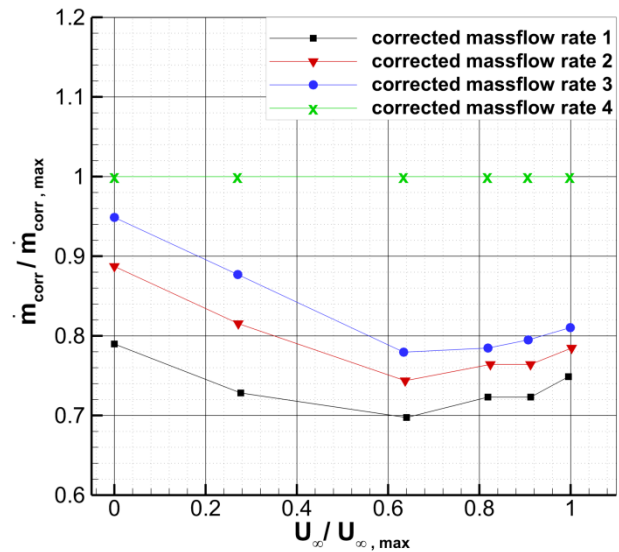


Fig. 7: Specified mass flow rate ( $\dot{m}_{corr} / \dot{m}_{corr, max}$ ) as function of specified freestream velocity ( $U_\infty / U_{\infty, max}$ ).

## 4. GEOMETRIC CONFIGURATIONS

### 4.1. Engine intake variants

Three different engine air intakes (EAI) are investigated. In Fig. 8, the baseline intake variants investigated in the wind tunnel campaign are depicted. Baseline variant 1 (BSL 1) is developed as a static intake. The second baseline intake variant (BSL 2) is designed as a “semi-dynamic” intake. For a better dynamic pressure recovery a ramp is included upstream of the intake opening. The optimization is considered for level flight conditions.

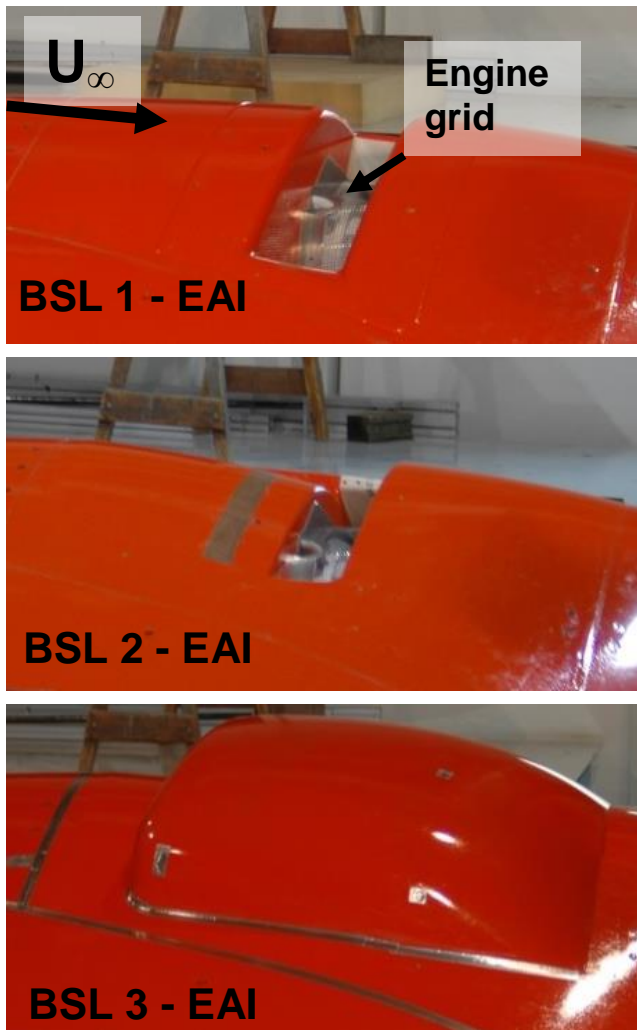


Fig. 8: Three baseline intake geometries.

The third baseline air intake (BSL 3) comprises the same main geometry of BSL 2 and a scoop. All three intakes feature an area-contraction between the entry and the engine face, which greatly helps to achieve low loss in hover flight conditions, Ref. [3].

#### 4.2. Engine plenum chamber variants

Two different baseline engine plenum chamber variants (EPC) are tested. The BSL 1 version of the EAI is tested with the BSL 1 of the EPC, as shown in Fig. 9. Both the BSL 2 and 3 versions of the EAI are investigated in combination with the BSL 2 of the EPC. The BSL 2 of the EPC features an overall rounded shape compared to the BSL 1 version. As depicted in Fig. 9, the EPC connects the EAI with the engine intake duct (EID). In the following, “BSL 1” denotes the combination of the BSL 1 – EAI with the BSL 1 – EPC.

In analogy, “BSL 2” stands for the combination of the BSL 2 – EAI with the BSL 2 – EPC and “BSL 3” stands for the combination of the BSL 3 – EAI with the BSL 2 – EPC.

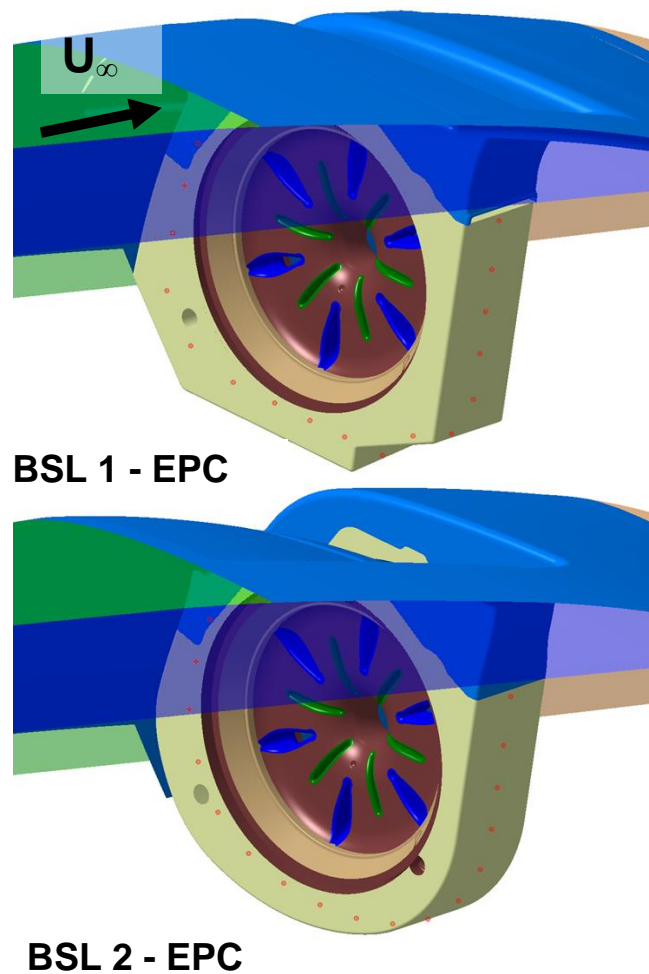


Fig. 9: Two baseline engine plenum chamber geometries.

To protect the engine from foreign objects, two wire grids are installed upstream of the engine. The intake grid is placed on the cowling, as depicted in Fig. 10 for the BSL 1 configuration. The cylindrical engine grid is located at the entry of the engine intake duct, as shown in Fig. 8. In order to separate the influence of the intake geometries from the grids' impact, the first comparison is carried out without intake grids. The influence of the intake grids is investigated for both the intakes 1 and 2.



Fig. 10: Baseline intake 1 with intake grid.

## 5. MEASUREMENT TECHNIQUE

### 5.1. 5-hole probe measurement

In order to optimize engine inflow conditions, total pressures and the 3 velocity components have been obtained in the AIP to determine aerodynamic engine installation parameters, such as total pressure losses, pressure distortion (e.g.  $DC_{60}$ ) and swirl. For this purpose, 5-hole probes were integrated in a rake at four radial positions, as depicted in Fig. 11. The rake is mounted on a shaft which is driven by a stepper motor and allows for the measurement in different circumferential positions  $\theta$ . The shaft is embedded in the EID front plate.

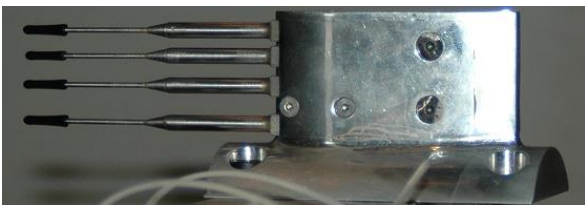


Fig. 11: 5-hole probes mounted in a rake.

The circumferential and radial distribution of the 5-hole probe measurement locations in the AIP is given in Fig. 12. Hereby, the X-axis and the engine axis are collinear. The Z-axis points at the guide vane (orange) which is situated in the middle of the intake opening (red). The Y-axis creates a right-hand system with the X- and Z- axes. The  $\theta$  angles are positive in clockwise direction. The procedure of calculating the three velocity components at each position based on the five pressures measured with a 5-hole probe is explained in Ref. [4].

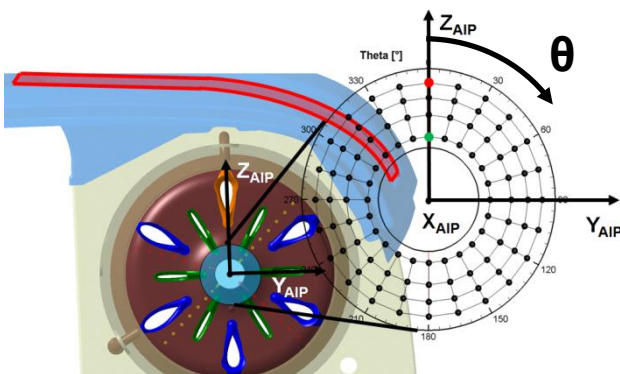


Fig. 12: Schematic overview of 5-hole-probe measurement locations in the AIP, view in upstream direction.

### 5.2. Static pressure measurement

Static pressure measurements at a total of 192 positions are conducted, of which 12 positions provide information about the transient pressures. In this paper only the distribution of mean surface pressures is evaluated. Pressure taps are located in 8 lines along the surface of the outer geometry, as depicted in Fig. 13. Further pressure taps are defined on 9 lines along the surface of the inner parts of the geometry, see Fig. 14. Line 9 is located in the mid plane of the EPC. In each of the circumferential positions  $\theta=45^\circ$ ,  $135^\circ$ ,  $225^\circ$  and  $288^\circ$  two lines are located, one on the EID front side and one on the EID back side.

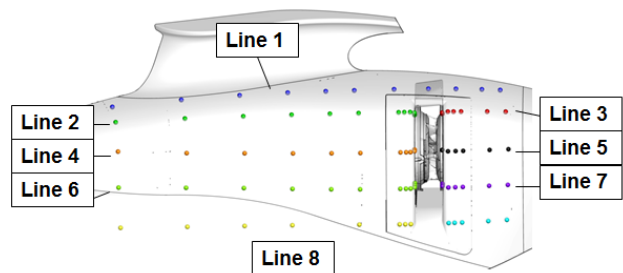


Fig. 13: Top view of pressure tap positions on the outer geometry of BSL 1.

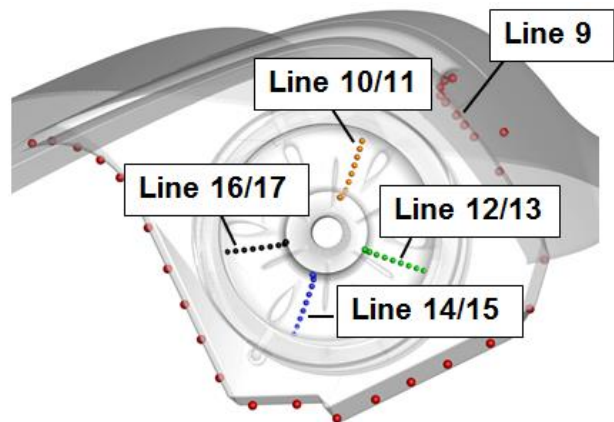


Fig. 14: Back view of pressure tap positions on the inner geometry of BSL 1.

For each line, a local curve length coordinate  $S$  is defined. The coordinate  $S$  ranges from 0 to 1 and is orientated along the surface in the mainstream direction. In Fig. 15 and Fig. 16, longitudinal cuts through the model at lines 2 and 3 are shown exemplarily together with the coordinate  $S$  (black for BSL 1, red for BSL 2) for the surface pressure tap locations (green dots).

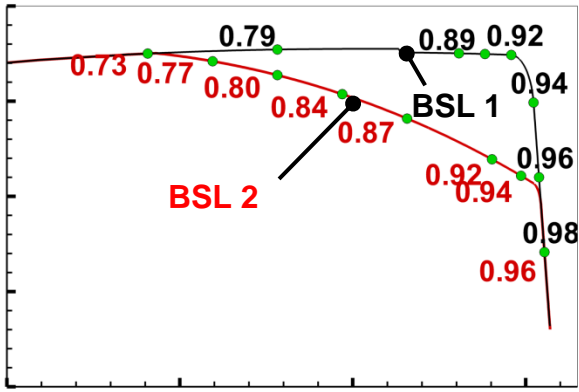


Fig. 15: Local curve length coordinate  $S_2$  for line 2 of BSL 1, 2.

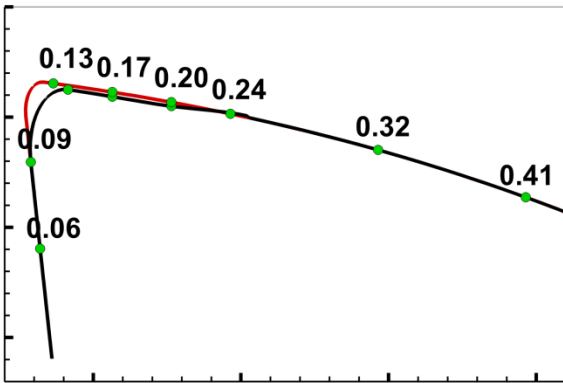


Fig. 16: Local curve length coordinate  $S_3$  for line 3 of BSL 1, 2.

The surface pressure distribution  $c_p$  is plotted over the local curve length coordinate  $S$ .  $c_p$  is defined as

$$(2) \quad c_p = \frac{p - p_\infty}{q_\infty}$$

The dynamic pressure  $q_\infty = \rho_\infty / 2 \cdot U_\infty^2$  is measured with a Prandtl probe at the nozzle exit.

## 6. EXPERIMENTAL RESULTS

### 6.1. AIP coefficients

Different coefficients are defined for the evaluation of the aerodynamic characteristics of the three baseline intakes depending on the engine operation conditions.

For the investigation of the intake's efficiency of the ram compression, a normalized total pressure ratio  $\eta_{norm}$  is defined, Ref. (3).

All total pressure ratios are normalized using the total pressure ratio  $\eta_{Ref}$ .

$$(3) \quad \eta_{norm} = \frac{\bar{p}_{t,AIP}}{p_{t,\infty}} \cdot \frac{1}{\eta_{Ref}}$$

$\bar{p}_{t,AIP}$  is the mean total pressure in the AIP.  $p_{t,\infty}$  is the total pressure at the nozzle exit. To examine the non-uniformity of the total pressure in the AIP the total pressure distortion is evaluated in accordance to Ref. [5]. Here, a normalized  $DC_{60,norm}$  coefficient is defined as

$$(4) \quad DC_{60,norm} = \frac{\bar{p}_{t,low} - \bar{p}_{t,AIP}}{\bar{q}_{AIP}} \cdot \frac{1}{DC_{60,Ref}}$$

The total pressure distortion level in the AIP is an indicator for stable engine operation [6]. The  $DC_{60}$  gives the difference of the lowest average total pressure  $\bar{p}_{t,low}$  segment with extent  $\theta = 60^\circ$  and the mean total pressure  $\bar{p}_{t,AIP}$  in the AIP and divides it by the mean AIP dynamic pressure  $\bar{q}_{AIP}$ . All values are normalized using the total pressure distortion  $DC_{60,Ref}$ . The influence of the freestream velocity on the total pressure losses is presented for the three baseline intakes. For that aim, the  $\eta_{norm}$  characteristics of the constant maximum mass flow rate  $\dot{m}_{corr,4}$  are shown in Fig. 17. The higher  $\eta_{norm}$  values of the BSL 2 for  $U_\infty / U_{\infty, max} > 0.24$  compared to the static side intake of BSL 1 shows the ram effect due to the ramp. The biggest relative difference of  $\Delta\eta_{norm,rel,1 \rightarrow 2} = 0.33\%$  appears for the highest velocity.

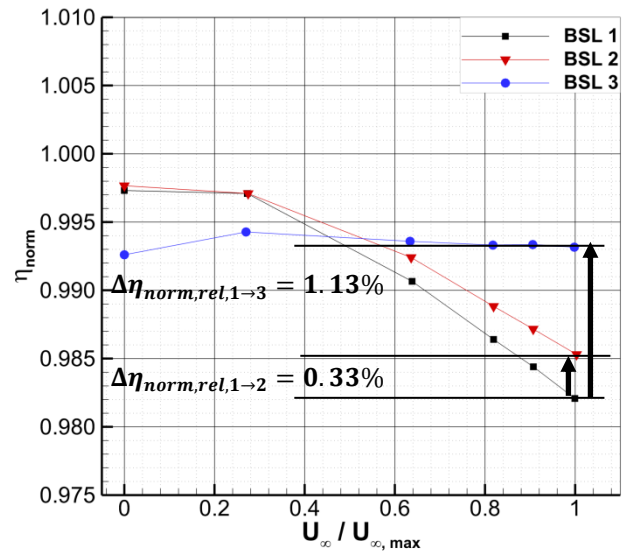


Fig. 17 Normalized total pressure ratio vs freestream velocity of the baseline intakes for  $\dot{m}_{corr,4}$ .

With the help of the scoop, the BSL 3 variant provides the best pressure recovery compared to the other intakes for the velocity range of  $U_\infty / U_{\infty, max} > 0.5$ . Again, the biggest relative difference of

$\Delta\eta_{norm,rel,1\rightarrow3} = 1.13\%$  appears for the highest velocity. For this intake,  $\eta_{norm}$  is nearly independent of  $U_\infty / U_{\infty, max}$ . Fig. 18 depicts the overall levels of  $\eta_{norm}$  for the different engine mass flow rates at the maximum freestream velocity.

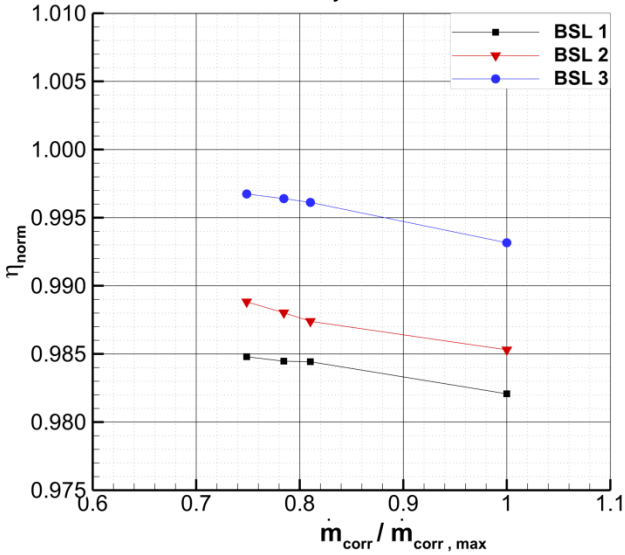


Fig. 18: Normalized total pressure ratio vs mass flow rate of the baseline intakes for  $U_\infty, max$ .

A nearly linear increase of total pressure losses, i.e. a linear decrease in  $\eta_{norm}$ , appears for the three intakes with very similar gradients. As shown in Fig. 19, for the BSL 1 and 3 configurations,  $DC_{60,norm}$  is nearly identical for the lower velocities. For the higher velocities, BSL 1 and BSL 2 have a very similar curve progression, but BSL 2 shows a slightly lower pressure distortion in the AIP. Overall, the BSL 3 produces the lowest variation and level of  $DC_{60,norm}$  for the engine operation range.

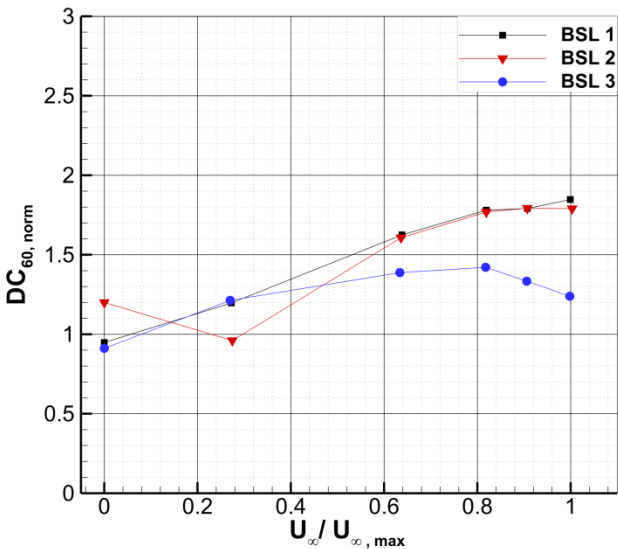


Fig. 19: Normalized distortion coefficient vs freestream velocity of the baseline intakes for  $\dot{m}_{corr,A}$ .

Regarding the  $DC_{60,norm}$  characteristics in Fig. 20, the BSL 3 intake is nearly independent of a variation of the engine mass flow rate for the highest freestream velocity tested. For both the BSL 1 and 2 the  $DC_{60,norm}$  decreases linearly with rising mass flow rates. The BSL2 variant reduces the  $DC_{60,norm}$  compared to the BSL 1 by a relative difference of  $\Delta DC_{60,norm,rel,1\rightarrow2} = -3.1\%$ . Generally, from the  $DC_{60,norm}$  point of view, with the BSL 3 intake the most stable engine operation is possible in the velocity spectrum tested. It reduces the  $DC_{60,norm}$  compared to the BSL 1 by a significant relative difference of  $\Delta DC_{60,norm,rel,1\rightarrow3} = -32.9\%$ .

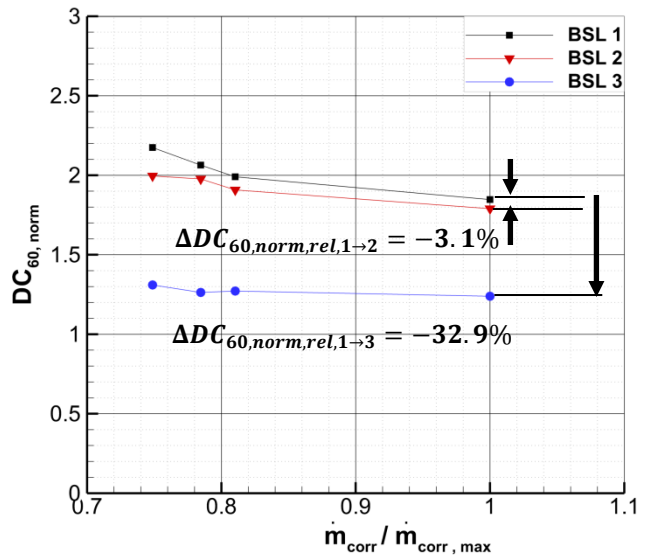


Fig. 20: Normalized distortion coefficient vs freestream velocity of the baseline intakes for  $U_\infty, max$ .

## 6.2. AIP flow field

In the following section with the use of the  $\eta_{norm}$  distributions in the AIP, additional investigations are shown for two combinations of  $U_\infty$  and  $\dot{m}_{corr}$ . For these, the biggest differences in  $\eta_{norm}$  and  $DC_{60,norm}$  appeared for the comparison of the three intakes. The first operation point is  $U_\infty / U_{\infty,max} = 0$ ,  $\dot{m}_{corr} / \dot{m}_{corr,max} = 1$ . The area of high level of  $\eta_{norm}$  as well as the overall level increases in the order of BSL 3, BSL 2 and BSL 1, as shown in Fig. 22 a) – c). Generally, in the area of the AIP between  $90^\circ < \theta < 270^\circ$ ,  $\eta_{norm}$  is low. The air which enters the EID in this angle regime has passed through several very turbulent regions of the flow field already in the EPC. Thus, its total pressure is low. In the upper part of the AIP, the  $\eta_{norm}$  shows the highest values due to the fact that in this part mainly air from the rather undisturbed freestream flow is ingested. The regions of the highest losses are very similar for the BSL 1 and BSL 2, while the BSL 3 has a much lower minimal total pressure level. Thus, the BSL 3

features the most homogeneous  $\eta_{norm}$ - distribution. The similarity of the  $DC_{60,norm}$  for the BSL 1 and 3 cannot be identified visually from the  $\eta_{norm}$  AIP distribution.

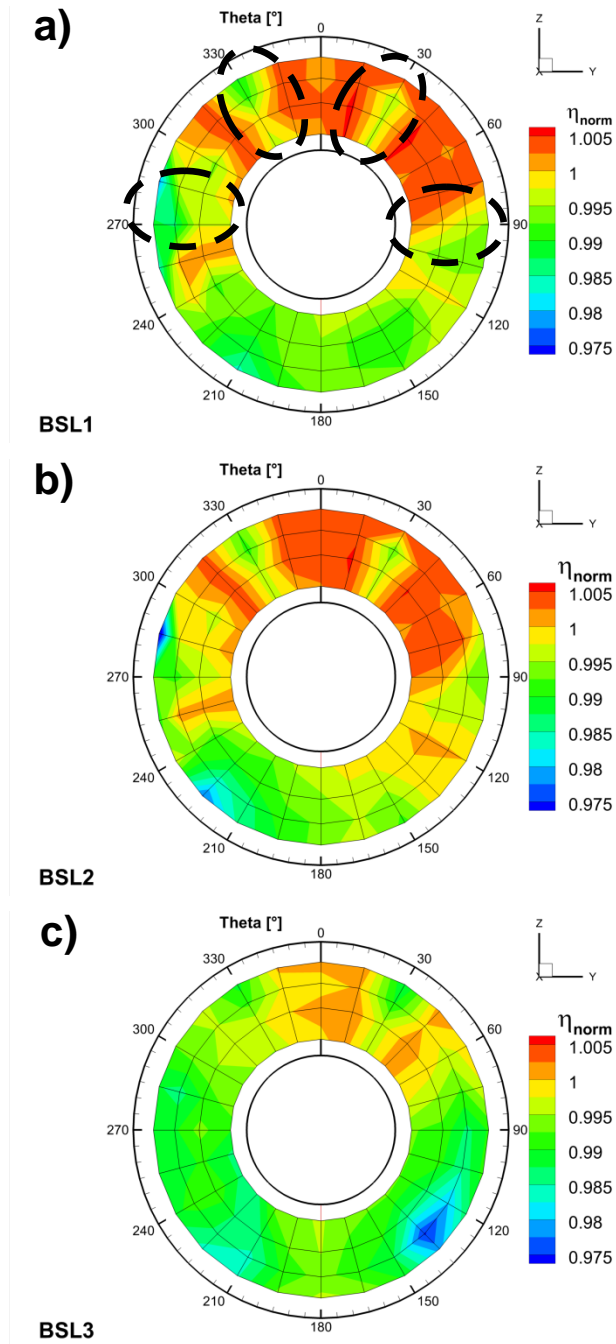


Fig. 21: Distribution of  $\eta_{norm}$  in AIP for a) BSL 1, b) BSL 2, c) BSL 3,  $U_{\infty} / U_{\infty, \max} = 0$ ,  $\dot{m}_{corr} / \dot{m}_{corr, \max} = 1$ .

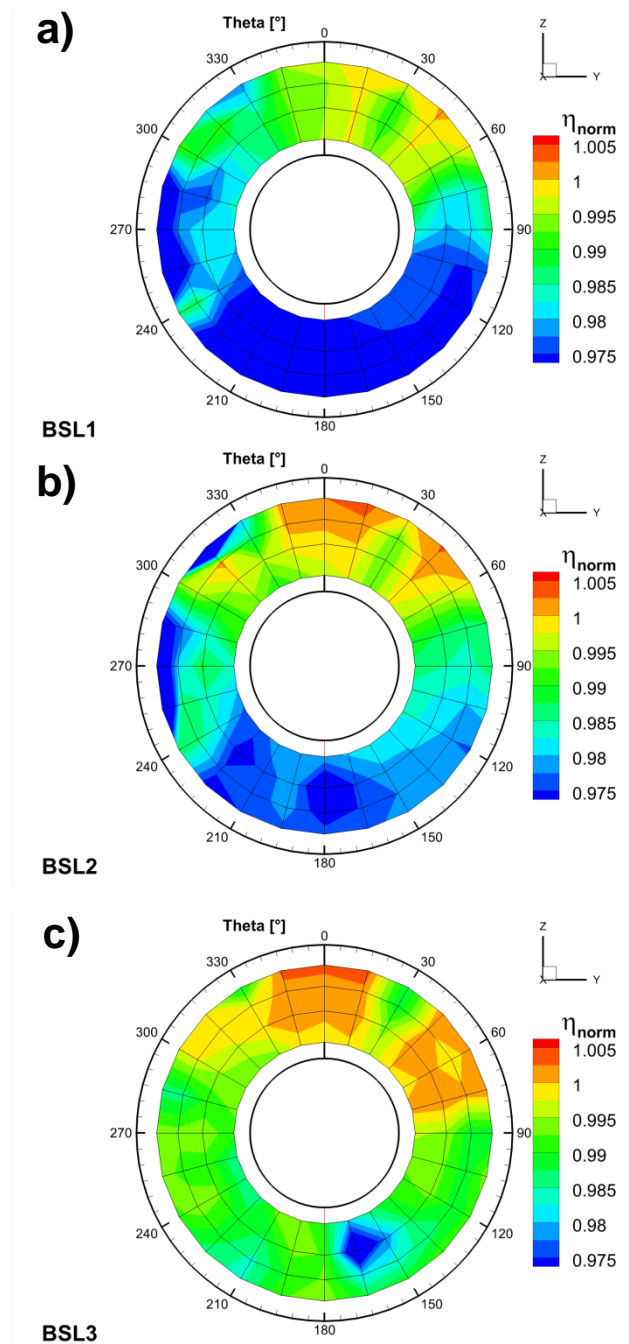


Fig. 22: Distribution of  $\eta_{norm}$  in AIP for a) BSL 1, b) BSL 2, c) BSL 3,  $U_{\infty} / U_{\infty, \max} = 1$ ,  $\dot{m}_{corr} / \dot{m}_{corr, \max} = 1$ .

The second operation point is characterized by  $U_\infty/U_{\infty,max} = 1$ ,  $\dot{m}_{corr}/\dot{m}_{corr,max} = 1$ . For both operation points, in the AIP, especially in the region of high dynamic pressures, wakes of the EID guide vanes are visible for  $\theta = 30^\circ, 90^\circ, 270^\circ$  and  $330^\circ$ . These are shown exemplarily in Fig. 21 a) and marked with a black dashed circle. For the second operation point, the trend is reversed, the area of high  $\eta_{norm}$  as well as the overall level increases in the order of BSL 1, BSL 2 and BSL 3, as depicted in Fig. 23 a) – c). This reflects the trend of the  $\eta_{norm}$  coefficient of Fig. 17. Again, the regions of the highest losses are qualitatively very similar for the BSL 1 and BSL 2. The BSL 3 has a much higher minimal pressure level in comparison to the two other intakes. The nearly identical  $\eta_{norm}$  distributions for the two operation points of the BSL 3 variant are in accordance with the little variation of  $\eta_{norm}$  and  $DC_{60,norm}$ , see Fig. 17 and Fig. 19, respectively.

### 6.3. Static pressure measurements

Selected surface pressure distributions are shown to give a better understanding of the flow field of the operation point of  $U_\infty/U_{\infty,max} = 1$  and  $\dot{m}_{corr}/\dot{m}_{corr,max} = 1$ . Additionally, for each  $c_p$  – plot a detail plot of the corresponding geometry is given. As depicted in Fig. 23 and Fig. 24, the lines 2 – 3 represent the cowling pressure distributions. For the BSL 3, between  $S_2 = 0.73 - 0.94$ , a part of the dynamic pressure can be turned to static pressure by the use of BSL 3's scoop ( $c_p \approx 0 \rightarrow 0.5$ ), see Fig. 23.

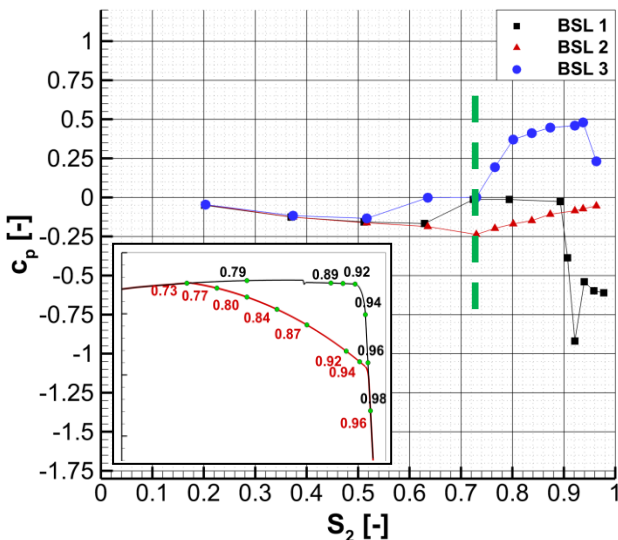


Fig. 23: Pressure distributions, line 2, baseline intakes 1-3,  $U_\infty / U_{\infty,max} = 1$ ,  $\dot{m}_{corr}/\dot{m}_{corr,max} = 1$ .

With the ramp of BSL 2 (start of ramp shown with green dashed line in Fig. 23), an increase in static pressure can be achieved from  $c_p = -0.25$  to

$c_p \approx -0.1$ . The air is accelerated around the upstream inlet lip of BSL 1's side intake. This leads to a pressure decrease for  $S_2 = 0.89 - 0.92$ . The pressure plateau at  $c_p \approx -0.6$  that appears in between  $S_2 = 0.94 - 0.98$  indicates a separation region. In Fig. 24, the pressure distributions of the intakes are shown for line 3.

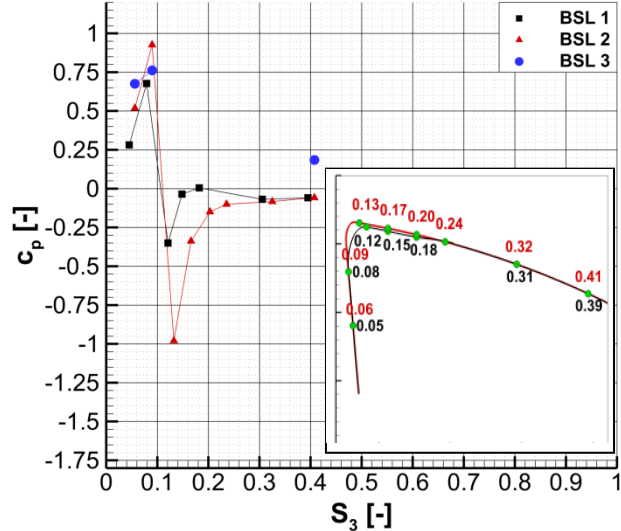


Fig. 24: Pressure distributions, line 3, baseline intakes 1-3,  $U_\infty / U_{\infty,max} = 1$ ,  $\dot{m}_{corr}/\dot{m}_{corr,max} = 1$ .

On the backward face of the inlet, a stagnation area appears between  $S_3 = 0.05 - 0.1$ . The stagnation area separates the air that enters the intake from that which is accelerated around the inlet lip and leads to a static pressure drop until  $c_p \approx -1$  at the position  $S_3 = 0.13$ . Some pressure taps are covered for the BSL 3 variant due to the scoop.

For the three intakes the pressure differences in the plenum chamber are nearly unchanged compared to the entry face of the intake, see Fig. 25.

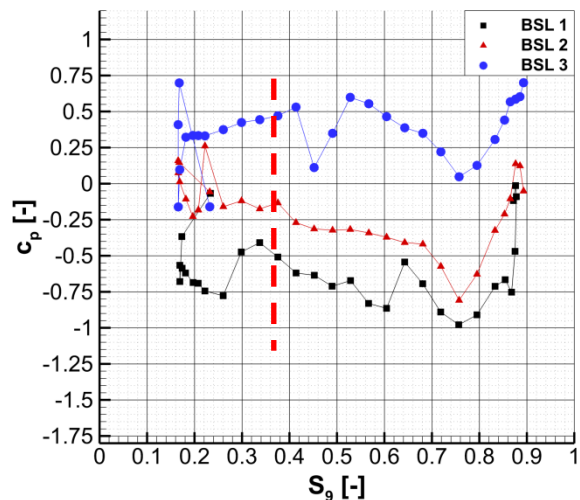


Fig. 25: Pressure distributions, line 9, baseline intakes 1-3,  $U_\infty / U_{\infty,max} = 1$ ,  $\dot{m}_{corr}/\dot{m}_{corr,max} = 1$ .

The lines 12 and 13, for which the  $c_p$ -distributions are shown in Fig. 26 and Fig. 27, are located at the angle position  $\theta = 135^\circ$  and  $S_9 = 0.375$ , respectively. These lines represent the EID geometry, which is identical for all intakes and rotationally symmetrical around the engine axis. The corresponding upstream plenum pressure values are highlighted using a red dashed line in Fig. 25.

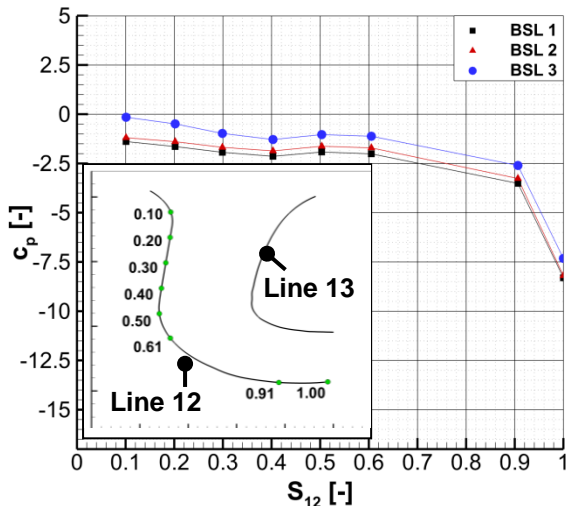


Fig. 26: Pressure distributions, line 12, baseline intakes 1-3,  $U_\infty / U_{\infty, \max} = 1$ ,  $\dot{m}_{\text{corr}} / \dot{m}_{\text{corr}, \max} = 1$ .

The tendency of the pressure curves is very similar for all three intake variants. The EID acts as a nozzle with a strong area contraction from entry to exit (AIP), which leads to a strong static pressure drop. As the front part of the EID (line 12) has a concave curvature, the contraction of the EID cross section does not lead to a strong static pressure drop on this surface. Due to a convex curvature, the flow is accelerated significantly on the back side of the EID as shown in Fig. 27.

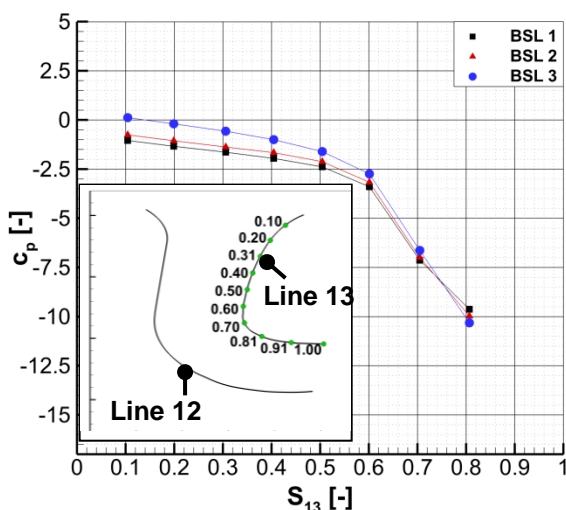


Fig. 27: Pressure distributions, line 13, baseline intakes 1-3,  $U_\infty / U_{\infty, \max} = 1$ ,  $\dot{m}_{\text{corr}} / \dot{m}_{\text{corr}, \max} = 1$ .

## 7. CONCLUSIONS

From the baseline wind tunnel campaign of the ATHENAI project first experimental results are shown. 5-hole pressure measurement data in the AIP (Aerodynamic Interface Plane) as well as surface pressure distributions are analyzed.

An emphasis is put on the effect of the three baseline's intake variants on the normalized total pressure ratio  $\eta_{\text{norm}}$  and the normalized total pressure distortion coefficient  $DC_{60, \text{norm}}$ . The BSL 1 intake is designed as a static intake with the purpose to minimize total pressure losses in the engine entry face for low speed and hover flight conditions. The BSL 3 intake is optimized for the fast level flight condition. For this aim a scoop is used which provides better dynamic to static pressure recovery and leads to the highest  $\eta_{\text{norm}}$  values of the three intakes for high velocities ( $\Delta\eta_{\text{norm}, \text{rel}, 1 \rightarrow 3} = 1.13\%$ ).

$\eta_{\text{norm}}$  of BSL 3 stays nearly constant for the engine operating conditions. For the low velocity regime, the BSL 1 and 2 variant show significantly lower pressure losses compared to the BSL 3 intake. Overall, the BSL 3 intake shows the lowest and nearly constant values of  $DC_{60, \text{norm}}$ . The  $DC_{60, \text{norm}}$  coefficient increases with higher velocities and decreases with a rise of the mass flow rate for the BSL 1 and 2 configurations. Here, the relative difference of the BSL 3 compared to the BSL 1 is  $\Delta DC_{60, \text{norm}, \text{rel}, 1 \rightarrow 3} = -32.9\%$ . With its ramp and uncovered inlet opening the BSL 2 intake is a good compromise of the BSL 1' hover flight advantages and the BSL 3's fast forward flight characteristics.

Based on this results the BSL 2 intake is chosen for further optimizations carried out in the course of the second ATHENAI project period. The optimization includes testing of retrofit solutions for the BSL 2 configuration such as spoilers, guide vanes and splitters, which are tested in a second wind tunnel campaign.

Additionally, numerical analyses are conducted to provide further information on the detailed flow phenomena in the intake region for the different intake shapes.

## Acknowledgment

The research project ATHENAI is funded within the European Community's Seventh Framework Program (FP/2007-2013) for the Clean Sky Joint Technology Initiative under grant agreement number 619819. The authors would like to thank the project partner Airbus Helicopters Deutschland GmbH for the support and the successful cooperation.

## References

- [1] Lehrstuhl für Aerodynamik und Strömungsmechanik der TU München. <http://www.aer.mw.tum.de>.
- [2] DIN e.V., DIN EN ISO 5167-4:2004-01, Durchflussmessung von Fluiden mit Drosselgeräten in voll durchströmten Leitungen mit Kreisquerschnitt. Berlin: Beuth Verlag GmbH, 2004.
- [3] Goldsmith E.L., Seddon J., Intake Aerodynamics. Kent: Collins Professional and Technical Books, 1985.
- [4] Yang Y., Rediniotis O., Telionis D., "Recent Developments in Multi-Hole Probe (MHP) Technology," in 20th International Congress of Mechanical Engineering. Vol. 21., 2009.
- [5] Welte D., "Experimental Analysis of a Pitot-Type Air Intake," Journal of Aircraft, vol. 23, no. 4, 1986.
- [6] AGARD, "Air Intakes for High Speed Vehicles," Neuilly-sur-seine, 1991.
- [7] Breuer T., Bissinger N. C., "Basic Principles–Gas Turbine Compatibility–Intake Aerodynamic Aspects," in Encyclopedia of Aerospace Engineering.: John Wiley & Sons, 2010, ch. Chapter EAE487.